The Astrophysical Journal, 943:13 (10pp), 2023 January 20 https://doi.org/10.3847/1538-4357/aca96c

The Late Afterglow of GW170817/GRB 170817A: A Large Viewing Angle and the Shift of the Hubble Constant to a Value More Consistent with the Local Measurements

Yi-Ying Wang[1,2], Shao-Peng Tang[1], Zhi-Ping Jin[1,2], and Yi-Zhong Fan[1,2]
[1] Key Laboratory of Dark Matter and Space Astronomy, Purple Mountain Observatory, Chinese Academy of Sciences, Nanjing 210033, People's Republic of China
yzfan@pmo.ac.cn, jin@pmo.ac.cn
[2] School of Astronomy and Space Science, University of Science and Technology of China, Hefei, Anhui 230026, People's Republic of China
Received 2022 August 18; revised 2022 December 5; accepted 2022 December 5; published 2023 January 20

Abstract

The multimessenger data of neutron star merger events are promising for constraining the Hubble constant. So far, GW170817 is still the unique gravitational wave event with multiwavelength electromagnetic counterparts. In particular, its radio and X-ray emission have been measured in the past ∼3–5 yr. In this work, we fit the long-lasting X-ray, optical, and radio afterglow light curves of GW170817/GRB 170817A, including the forward shock radiation from both the decelerating relativistic gamma-ray burst outflow and the subrelativistic kilonova outflow (though whether the second component contributes significantly is still uncertain), and find out a relatively large viewing angle (∼0.5 rad). Such a viewing angle has been taken as a prior in the gravitational wave data analysis, and the degeneracy between the viewing angle and the luminosity distance is broken. Finally, we have a Hubble constant $H_0 = 72.57^{+4.09}_{-4.17}$ km s^{-1} Mpc^{-1}, which is more consistent with that obtained by other local measurements. If rather similar values are inferred from multimessenger data of future neutron star merger events, it will provide critical support to the existence of the Hubble tension.

Unified Astronomy Thesaurus concepts: Hubble constant (758); Gravitational wave astronomy (675); Gamma-ray bursts (629)

1. Introduction

The Hubble constant (H_0) is a fundamental parameter of cosmology. However, its measurements obtained with different methods are clustered into two groups (Verde et al. 2019): one is represented by the cosmic microwave background (CMB) measurement from the Planck Collaboration for the early universe (67.66 ± 0.42 km s^{-1} Mpc^{-1}; Planck Collaboration et al. 2020) and the other is represented by the type Ia supernova and Cepheids measurements from the SHOES (Supernova, H_0, for the Equation of state of Dark Energy) team in the local universe (73.30 ± 1.04 km s^{-1} Mpc^{-1}; Riess et al. 2022). So far, it is still unclear whether such a severe tension is due to the presence of new physics (i.e., the modification of the standard cosmology model) or alternatively some unknown systematic bias introduced in the local measurements (Dainotti et al. 2021, 2022). Independent precise local H_0 measurements without using the distance ladders are thus necessary to check the second possibility. The gravitational wave (GW) events are expected to play an important role in such an aspect since GWs, serving as the standard siren, can be used to measure H_0 (Schutz 1986). This is particularly the case for the neutron star merger events with detected multiwavelength electromagnetic counterparts. For such events, the redshifts can be reliably measured, and the inclination angles (i.e., the viewing angle) of the mergers may be robustly inferred. Therefore, the degeneracy between the luminosity distance and the inclination angle can be effectively broken. The accurate redshift and luminosity distance thus lead to a direct measurement of H_0.

The multimessenger data of GW170817 (Abbott et al. 2017b, 2019) have been extensively used to estimate the Hubble constant. Abbott et al. (2017a) took the strain data and the redshift measurement of GW170817 to measure H_0, which was determined to be $70^{+12.0}_{-8.0}$ km s^{-1} Mpc^{-1}. Later, the inclusion of the electromagnetic radiation information yields a more accurate measurement of H_0, as reported in the literature. For instance, Hotokezaka et al. (2019) took both the superluminal motion and the multiwavelength radiation of the relativistic jet into account and yielded a viewing angle of $0.29^{+0.03}_{-0.02}$ rad for the power-law jet model, with which a $H_0 = 68.1^{+4.5}_{-4.3}$ km s^{-1} Mpc^{-1} is reported. Wang & Giannios (2021) found that $H_0 = 69.48^{+4.3}_{-4.2}$ km s^{-1} Mpc^{-1} when further including the direct measurement of the luminosity distance. There are also some constraints reported from other literature, e.g., $H_0 = 64.8^{+7.3}_{-7.2}$ km s^{-1} Mpc^{-1} (Howlett & Davis 2020), $H_0 = 66.2^{+4.4}_{-4.2}$ km s^{-1} Mpc^{-1} (Dietrich et al. 2020), and $H_0 = 68.3^{+4.6}_{-4.5}$ km s^{-1} Mpc^{-1} (Mukherjee et al. 2021). Though the uncertainties are relatively large, their median values are close to those found in the CMB, baryon acoustic oscillations, and big bang nucleosynthesis experiments (Abbott et al. 2018).

However, in the previous afterglow-involved H_0 measurements, only the first-year afterglow data of GRB 170817A have been included in the modeling (for instance, Wang & Giannios 2021 just fitted the afterglow data collected in the first 200 days to infer the viewing angle of the gamma-ray burst (GRB) ejecta due to the lack of reliable treatment on the sideways expansion in the code). Currently, the afterglow observations of GRB 170817A have been accumulated to almost 4.8 yr (O'Connor & Troja 2022). These late time afterglow data are expected to constrain the physical parameters tightly. Interestingly, it is found that the viewing angle θ_v of the GRB ejecta (which is widely assumed to be the same as the inclination angle ι of the merger event) gets

increased if the late time data have been included in the fit (Hajela et al. 2019; Nathanail et al. 2021; Hajela et al. 2022). Therefore, it is necessary to fit all the available afterglow data to yield a more reliable θ_v (i.e., ι). Besides, the superluminal motion of a relativistic jet of GW170817 (Mooley et al. 2018a; Hotokezaka et al. 2019; Ghirlanda et al. 2019) that provides an extra constraint on θ_v will also be incorporated in this work. By performing the Bayesian analysis on both the multiwavelength light curves and GW data, we find that the Hubble constant is $H_0 = 72.57^{+4.09}_{-4.17}$ km s^{-1} Mpc^{-1}, which is more consistent with that obtained by other local measurements.

2. The Afterglow Data

Recently, the synchrotron afterglow emission of GRB 170817A in the X-ray wavelength after 1674 days since the merger of GW170817, was detected (O'Connor & Troja 2022). Therefore, we incorporate this new observation with all of the available data in radio, optical, and X-ray bands into the afterglow modeling (which will be described in Section 3). In the radio band, the data cover the early and late duration from 16 to 1243 days after the binary neutron star (BNS) merger, which are obtained by the Karl G. Jansky Very Large Array (Hallinan et al. 2017; Mooley et al. 2018a; Margutti et al. 2018; Alexander et al. 2018), the Australia Telescope Compact Array (Hallinan et al. 2017; Mooley et al. 2018b, 2018c; Dobie et al. 2018; Makhathini et al. 2021), the Giant Metrewave Radio Telescope (Mooley et al. 2018b; Resmi et al. 2018), the enhanced Multi Element Remotely Linked Interferometer Network (Makhathini et al. 2021), the Very Long Baseline Array (Ghirlanda et al. 2019), and the MeerKAT telescope (Mooley et al. 2018b; Makhathini et al. 2021). In the optical band, the data distributed around the light-curve peak from 109 to 362 days postmerger are obtained by the Hubble Space Telescope (Lyman et al. 2018; Lamb et al. 2019; Fong et al. 2019). The observations in the X-ray band from the early (9 days) to the very late (1674 days) time after the merger are obtained by the XMM-Newton (D'Avanzo et al. 2018; Piro et al. 2019) and Chandra (Troja et al. 2017, 2018; Hajela et al. 2019; Troja et al. 2020; O'Connor & Troja 2022; Troja et al. 2022).

3. Method

As the only "standard siren" so far, the source of GW170817 is confirmed to be located in NGC 4993 (Abbott et al. 2017b). In the local universe, we have Hubble's law

$$v_H = v_r - v_p = H_0 d_L, \tag{1}$$

where v_H is the local Hubble flow velocity of the galaxy, v_r is the recession velocity of the galaxy relative to the CMB frame, and v_p is the peculiar velocity of the galaxy. Thus, the posterior probability of H_0 is

$$p(H_0|x_{GW}, \langle v_H \rangle) \propto p(H_0) \int \mathrm{d}d_L \mathrm{d}v_H p(v_H) p(\langle v_H \rangle | v_H) p(d_L|x_{GW}), \tag{2}$$

where $p(d_L|x_{GW})$ is the posterior distribution of d_L given by the Bayesian analysis on x_{GW}, and $p(\langle v_H \rangle | v_H)$ is the likelihood of the Hubble flow velocity measurement. Here, we use the result from Mukherjee et al. (2021), i.e., the velocity of the Hubble flow is $v_H = 2954 \pm 148.6$ km s^{-1} following a Gaussian distribution.

To obtain a high precision luminosity distance from the GW data analysis, we need to break the degeneracy between ι and d_L. Therefore, how to (independently) acquire a reliable measurement of ι is crucial. Assuming that the viewing angle θ_v in the GRB afterglow is equal to the inclination angle ι, an acknowledged method is to infer the angle by fitting multiwavelength light curves with afterglow models. In this work, we adopt two approaches (i.e., the `Afterglowpy` and `JetFit`) developed by Ryan et al. (2020) and Wu & MacFadyen (2018) to constrain θ_v, respectively. For `Afterglowpy`, multinumerical/analytic structured jet models are implemented for calculating GRB afterglow light curves and spectra. While for `JetFit`, since there are ~2,000,000 synchrotron spectra computed from the hydrodynamic simulations, the full parameter space for fitting the light curves can be well explored by Markov Chain Monte Carlo analysis (Wu & MacFadyen 2018). In this work, we take the model from Wu & MacFadyen (2018) as the fiducial one because the `Afterglowpy` code makes approximation[3] on the sideways expansion; moreover, the `JetFit`gives stronger Bayes evidence, as we will show below. Except for the GRB afterglow, the kilonova afterglow might become a dominant component (Hajela et al. 2022) at late times. Driven by the kilonova blast wave, the kilonova afterglow is caused by a shock through the external medium. Therefore, it can be approximated as a spherical cocoon model in the subrelativistic regime. Lately, Sarin et al. (2022) exploited an open source package `Redback` for fitting an electromagnetic transient. They approximated the kilonova afterglow as a spherical cocoon afterglow extended in `afterglowpy` but with some constraints. As shown in Table 1, we adopt the setting of the prior of the kilonova afterglow in `Redback` but import `afterglowpy` directly. More complicated models of the kilonova afterglow and further discussions can be found in Kathirgamaraju et al. (2019) and Nedora et al. (2021). Therefore, such a component, calculated with the `Afterglowpy` code, is also incorporated in our numerical fits.

We update the analysis with multiband light-curve data of GRB 170817A, including the data from radio and optical bands to X-ray bands, from 9.2 to 1674 days. Following Wu & MacFadyen (2018), the `JetFit` model in our work has eight free parameters. Their prior distributions are summarized in Table 1.[4] For other structured jet models in `Afterglowpy`, the priors are similar to those in Table 1. Additionally, the superluminal motion of the jet observed with Very Long Baseline Interferometry (VLBI) gives a constraint of $0.25 < \theta_v \left(\frac{d_L}{41\mathrm{Mpc}}\right) < 0.5$ rad (Mooley et al. 2018a). The likelihood of fitting the observation data (assuming the measurement error follows a Gaussian distribution) with the afterglow model in the Bayesian statistical framework can be written as

$$\text{Likelihood} = \prod_i^N \frac{1}{\sqrt{2\pi}\sigma_i} \exp\left[-\frac{1}{2}\left(\frac{f(x_i) - y_i}{\sigma_i}\right)^2\right], \tag{3}$$

[3] To simplify the calculation, `Afterglowpy` assumes a sideways expansion rate of the local sound speed. However, the numerical hydrodynamical simulations (Kumar & Granot 2003) revealed that the sideways expansion rate is usually lower than the speed of sound, which predicts shallower-decaying light curves at late times.

[4] The same as those in the Table 2 of Wu & MacFadyen (2018), except that the fraction of electrons accelerated by the shock is fixed to 1 and the luminosity distance d_L follows a Gaussian distribution with $\mu = 40.7$ and $\sigma = 2.36$ Mpc (Mukherjee et al. 2021).

Table 1
Prior Distributions of the Parameters for GRB 170817A and Kilonova Afterglow

Names	Parameters	Priors of Parameter Inference
Explosion energy	$\log_{10} E_{0,50}$ [a]	Uniform(−6, 7)
Circumburst density[b]	$\log_{10} n_{0,0}$ [a]	Uniform(−6, 0)
Asymptotic Lorentz factor	η_0	Uniform(2, 10)
Boost Lorentz factor	γ_B	Uniform(1, 12)
Spectral index[b]	p	Uniform(2, 2.5)
Electron energy fraction[b]	$\log_{10} \epsilon_e$	Uniform(−6, 0)
Magnetic energy fraction[b]	$\log_{10} \epsilon_B$	Uniform(−6, 0)
Viewing angle[b]	θ_v/rad	Sine(0, π)
Isotropic-equivalent energy[b]	$\log_{10} E_{iso}$/erg	Uniform(−44, 57)
Half-opening angle[b]	θ_c	Uniform(0, $\pi/2$)
Outer truncation angle[b]	θ_w	Uniform(0, $\pi/2$)
Luminosity distance[b]	d_L/Mpc	Gaussian ($\mu = 40.7$, $\sigma = 2.36$)
Maximum 4-velocity of outflow	U_{Max}	Uniform(0.15, 0.7)
Minimum 4-velocity of outflow	U_{Min}	Uniform(0.1, 0.15)
Normalization of outflow's energy distribution	E_r/erg	Uniform(45, 50)
Power-law index of outflow's injection	k	Uniform(0.5,4)
Mass of material at U_{Max}	$\log_{10}$(Eject mass)/$M_\odot$	Uniform(45, 50)
Spectral index	p	Uniform(2.0, 2.5)
Electron energy fraction	$\log_{10} \epsilon_e$	Uniform(−5, 0)
Magnetic energy fraction	$\log_{10} \epsilon_B$	Uniform(−5, 0)
Fraction of electrons that get accelerated	ξ_N	Uniform(0, 1)
Initial Lorentz factor	Γ_0	Uniform(1,0)

Notes.
[a] Note that, $E_{0,50} \equiv E_0/10^{50}$ erg and $n_{0,0} \equiv n_0/1$ proton cm^{-3}.
[b] These parameters are used in Gaussian structured jet in `Afterglowpy`.

where (x_i, y_i) and σ_i are the observed light-curve data and their uncertainties, respectively; $f(x_i)$ is the value predicted by the afterglow model at x_i. Balancing the accuracy and the efficiency, the Bayesian analysis of these afterglow parameters adopt `Pymultinest` as the sampler.

After obtaining the posterior distribution of inclination angle through the afterglow light-curve fitting, we can take the posterior distribution as a prior and input it into the Bayesian analysis of GW data. The priors of other GW parameters are shown in Table 2, where the prior of d_L follows the distribution obtained by Mukherjee et al. (2021). We assume that the BNS has aligned spins, and the precession effects can be neglected. As for the waveform template, we use the model of `IMRPhenomD_NRTidal` (Dietrich et al. 2019). The calibration uncertainties may slightly impact Hubble constant measurements (Huang et al. 2022). While for GW170817, we find that the difference between H_0 results obtained with and without considering calibration is negligible since the uncertainty of peculiar velocity still dominates the uncertainty of H_0. We calculate the marginalized posterior distribution of luminosity distance using the GW parameter inference code `Bilby` (Ashton et al. 2019) and adopt `dynesty` (Speagle 2020) as the nest sampler. Given a uniform prior distribution from 20 to 140 km s^{-1} Mpc^{-1}, the Hubble constant then can be well estimated using Equation (2) based on the tight constraint of the luminosity distance.

4. Result

We have systematically investigated the factors that might influence the determination of viewing angle, including the approaches (`Afterglowpy` and `JetFit`), the structured jet models (Gaussian, power-law, and top-hat structures), and the data sets (200 days/entire afterglow data and the VLBI's constraint). Figure 1 presents our optimal fitting with two different models. The posterior results shown in Figure 2 indicate that the superluminal motion of the jet gives a combined limitation between the viewing angle and the luminosity distance. In general, the inclusion of the late time (i.e., $\geqslant$200 days) afterglow data yields a larger viewing angle with a lower uncertainty, as anticipated (one exception is the superluminal motion constrains the viewing angle obtained in the `JetFit` model of all the afterglow data to be consistent with that of the first 200 days). Without the sideways lateral expansion, the logarithm of Bayes evidence ($\ln Z$) is 10 less than the Gaussian structured jet with expansion, suggesting a much poorer fit. For the `JetFit` model using the entire data set, the θ_v is constrained to $0.53^{+0.01}_{-0.01}$ rad (at the 68.3% credible level; other parameters of the afterglow model are presented in Table 1 and Figure 2, which is consistent to the results obtained by Nathanail et al. 2021). Using the same boosted-fireball model and similar data set, Hajela et al. (2022) instead found $\theta_v = 0.44^{+0.01}_{-0.01}$ rad. Such a difference is mainly due to the fixed $n_{0,0}$, γ_B, and ϵ_e in the afterglow modeling of Hajela et al. (2022). With `Afterglowpy`, the Gaussian structured jet model (the posterior results are shown in Figure 2) gives a $\theta_v = 0.51^{+0.01}_{-0.02}$ rad. For the `JetFit` and the `Afterglowpy` Gaussian structured jet models, the $\ln Z$ are 594 and 562, respectively. In comparison to the `Afterglowpy` Gaussian jet model, the power-law and top-hat models cannot well fit the observations, and the results are $\ln Z = 546$ ($\theta_v = 0.46^{+0.01}_{-0.01}$ rad) and 426 ($\theta_v = 0.50^{+0.03}_{-0.04}$ rad), respectively. All of the posterior distributions of these scenarios are presented in the Appendix. Therefore, we only display the best-fit light curves for the `JetFit` and Gaussian structured jet models in Figure 1. We would like to also comment on the role of the kilonova afterglow component. Though the inclusion of this component can improve the goodness of the fit, its existence cannot be convincingly established in the `JetFit` model, for which the enhancement of $\ln Z$ is just $\approx$4. In the `Afterglowpy` Gaussian jet model, the kilonova afterglow is more prominent and dominates the emission at $t \geqslant 700$ days. The corresponding posterior distribution is presented in the Appendix (the estimated parameters of kilonova afterglow do not show well the convergence if we use the `JetFit` model for the GRB afterglow). Motivated by its highest $\ln Z$ value, in this work we adopt the `JetFit` model as our fiducial approach. Nevertheless, the rather similar θ_v inferred in the above diverse approaches/models do consistently favor a large viewing angle of $\approx$0.5 rad. Another thing that should be mentioned is that the explosion energy we obtained is larger than that estimated in several early works (e.g., Lamb et al. 2019; Lin et al. 2019; Troja et al. 2019; Ryan et al. 2020), but is close to some recent evaluations (e.g., Nathanail et al. 2021; Hajela et al. 2022). Such high energy supports the claim that GRB 170817A would be one of the brightest short events

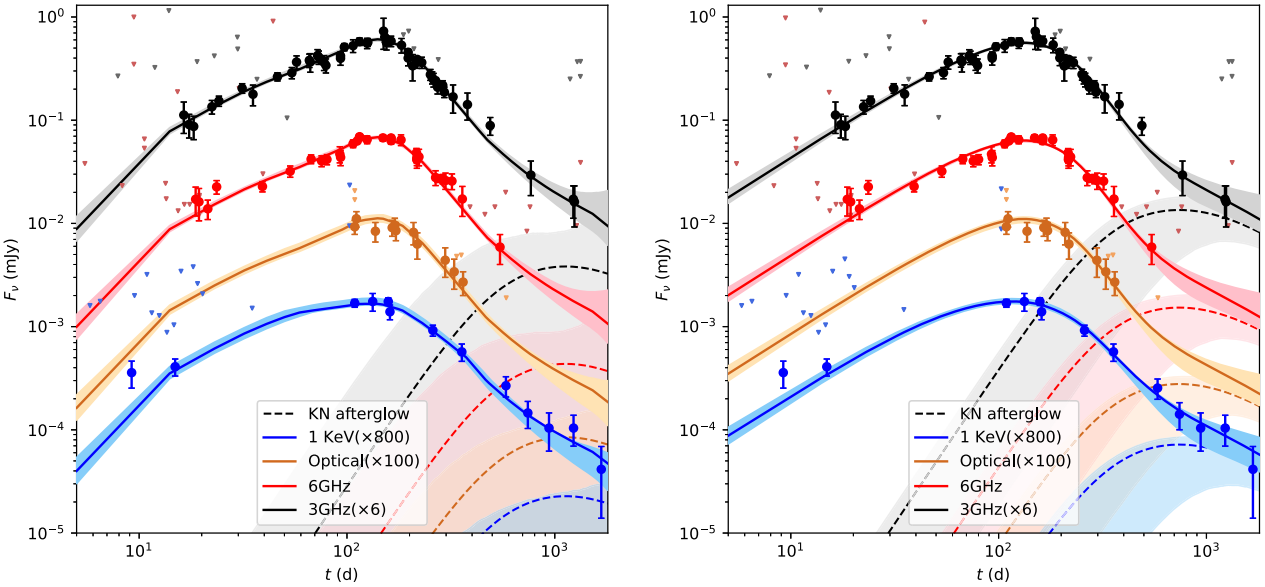

Figure 1. The fit to the afterglow data in the time interval of 5–1800 days after GW170817/GRB 170817A. Panels (a) and (b) show the reproduced light curves in two different methods, the boosted-fireball structured jet model (`JetFit`) and the Gaussian structured jet model (`Afterglowpy`). We denote the frequencies of 1 keV, 5.06×10^{14} Hz (optical), 6 GHz, and 3 GHz in black, red, brown, and blue, respectively. Here, each band's flux F_ν is rescaled for a better view. The solid lines (with maximum likelihood) represent the best fit of the whole afterglow data, including both the GRB and the kilonova afterglow components. The colored regions represent the corresponding 90% credible regions. The dashed lines are the kilonova afterglow components. The light-colored regions represent the 90% credible regions of the estimated kilonova light curves. The observation data points are marked in circles with error bars, and the upper limits are shown in lower triangles.

Table 2
Prior Distributions and Posterior Results of the Parameters for GW170817

Names	Parameters	Priors of Parameter Inference	Posterior Results[b]
Chirp mass	$\mathcal{M}/M_\odot$	Uniform(0.4, 4.4)	$1.1976^{+0.0001}_{-0.0001}$
Mass ratio	q	Uniform(0.125, 1.0)	$0.76^{+0.16}_{-0.17}$
Aligned spin	$\chi_{1,2}$	AlignedSpin[a]	$0.01^{+0.12}_{-0.09}$ & $0.02^{+0.16}_{-0.14}$
Polarization of GW	ψ	Uniform(0, 2π)	$1.60^{+1.04}_{-1.16}$
Coalescence time	t_c/s	1187008882.42	-
Coalescence phase	ϕ_c	Uniform(0, 2π)	Marginalized
Right ascension	α	3.44616	-
Decl.	δ	−0.408084	-
Tidal deformability	$\Lambda_{1,2}$	Uniform(0,5000)	204^{+342}_{-147} & 590^{+752}_{-344}
Inclination angle	ι /rad	Constrained by afterglow model analysis	$2.61^{+0.01}_{-0.01}$
Luminosity distance	d_L /Mpc	Gaussian($\mu = 40.7$, $\sigma = 2.36$)	$40.67^{+1.11}_{-1.03}$

Notes.
[a] The spin component projected to the orbit angular momentum follows the distribution described in Equation (A7) of Lange et al. (2018) with $\chi_{\rm max} = 0.89$, and the spin's tilt angle is taken to be aligned.
[b] The posterior results are at the 68.3% credible level.

detected so far (Duan et al. 2019). The inferred large θ_v points toward a high GRB/GW association rate and hence a promising multimessenger detection prospect of the double neutron star mergers in the future (Jin et al. 2018). Besides, we do not find evidence for the sizeable deviation of the model prediction from the data, which suggests that there is no sign of a continual energy injection from the central engine. Hence, it is in favor of a black hole rather than a neutron star central engine for GRB 170817A (see also Han et al. 2022, for an independent argument).

Then, we use the posterior distribution of the viewing angle $\theta_v = 0.53^{+0.01}_{-0.01}$rad obtained in the `JetFit` model ($\theta_v = 0.51^{+0.01}_{-0.02}$rad for the Gaussian jet model) as the prior of inclination angle in GW data analysis. The full Bayesian inference on GW170817 limits d_L to $40.67^{+1.11}_{-1.03}$ Mpc ($d_L = 41.09^{+1.19}_{-1.05}$ Mpc when using a Gaussian structured jet) at the 68.3% confidence level. The estimations of other GW parameters are shown in Table 2. Because of the breaking of the degeneracy between ι and d_L, GW analysis gives about 5.6% uncertainty on the Hubble constant and limits H_0 close to the SHOES result, i.e., $H_0 = 72.57^{+4.09}_{-4.17}$ km s^{-1} Mpc^{-1} ($H_0 = 71.80^{+4.15}_{-4.07}$ km s^{-1} Mpc^{-1} when using the Gaussian jet model) at the 68.3% credible level (see Figure 3). If inheriting both the estimated d_L and θ_v from afterglow fitting as the prior of GW analysis, we would have $H_0 = 75.52^{+4.09}_{-4.04}$ km s^{-1} Mpc^{-1} ($H_0 = 73.53^{+4.00}_{-3.96}$ km s^{-1} Mpc^{-1}) for the `JetFit` (Gaussian)

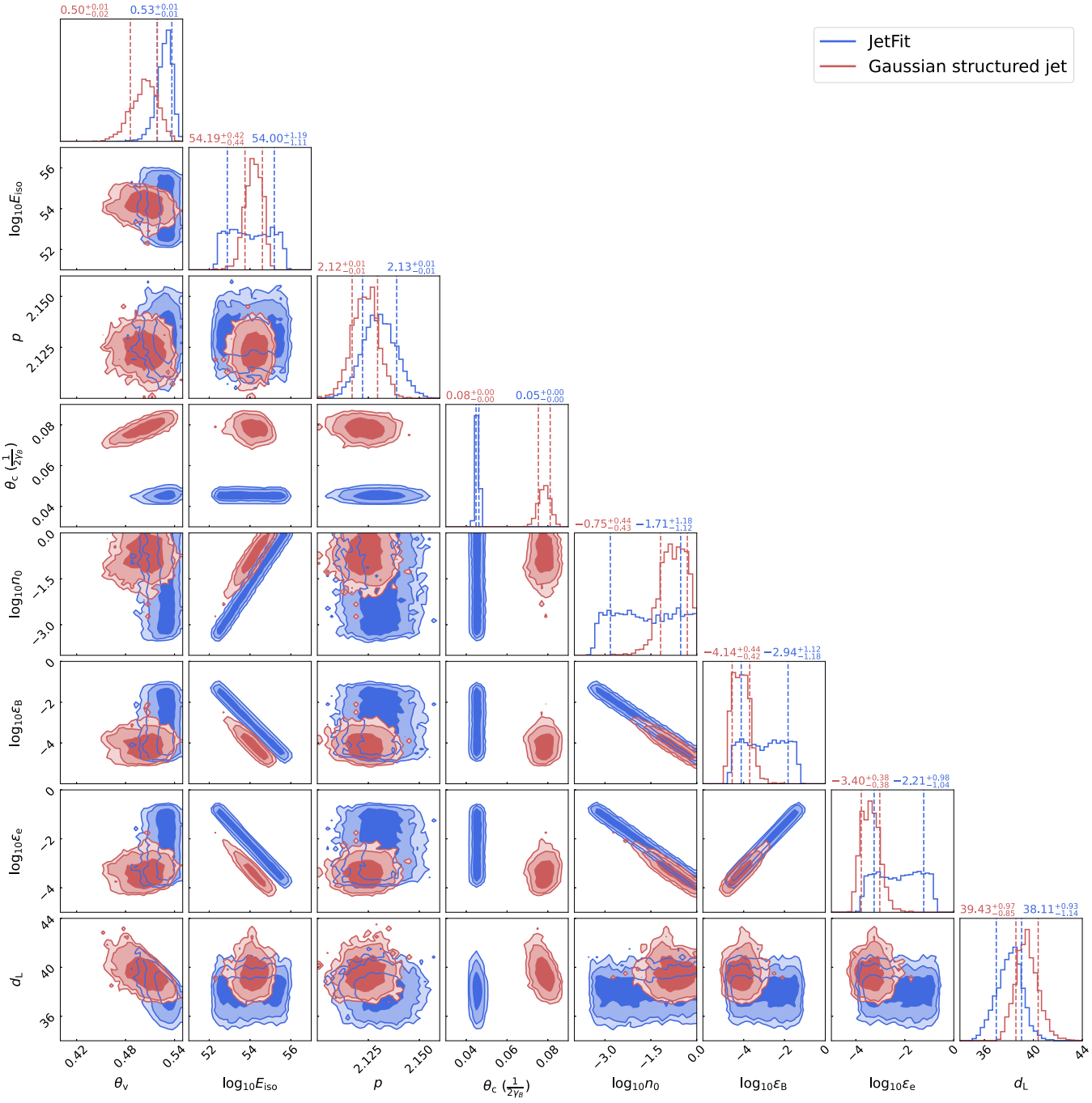

Figure 2. Posterior distributions of some key parameters for the best-fit light curves presented in Figure 1. The results of the `JetFit` and the Gaussian structured models are marked in blue and red, respectively. As the jet opening angel is $\sim 1/\gamma_B$ in the boosted-fireball model, we plot the half-opening angle θ_c and $1/2\gamma_B$ in the same corner for a convenient comparison. In `Jetfit` and Gaussian structured models, the energy of the GRB jet is described as the explosion energy E_0 and the isotropic-equivalent energy $E_{\rm iso}$ at $\theta = 0$, respectively. Considering $E_{\rm iso} \sim 2E_0/[1 - \cos(\theta_0/2)]$ (Wu & MacFadyen 2018), we convert E_0 to $E_{\rm iso}$ for a convenient comparison. The contours are at the 68%, 95%, 99% credible level. The values are at 68% credible level.

model, with which the difference from the Planck H_0 measurement is more distinct. One thing that should be mentioned is that if we do not take into account the constraint of the viewing angle, i.e., $0.25 < \theta_{\rm v}\left(\frac{d_{\rm L}}{41{\rm Mpc}}\right) < 0.5$ rad (Mooley et al. 2018c; Hotokezaka et al. 2019), in the afterglow modeling, $\theta_{\rm v}$ can still be well constrained but prefers a larger value ($\sim$0.6 rad in `JetFit` model) and hence a larger $d_{\rm L}$. Correspondingly, in comparison to the results considering the VLBI's constraint, we would yield a larger result $H_0 = 74.36^{+4.44}_{-4.32}$ km s^{-1} Mpc^{-1}, and the difference from the Planck H_0 measurement is more distinct, also.

5. Conclusion

For the GW event accompanying an electromagnetic counterpart, H_0 can be estimated by the standard siren method. This method utilizes redshift information from a confirmed host galaxy and the posterior distribution of luminosity distance from GW data analysis to obtain the H_0 value following

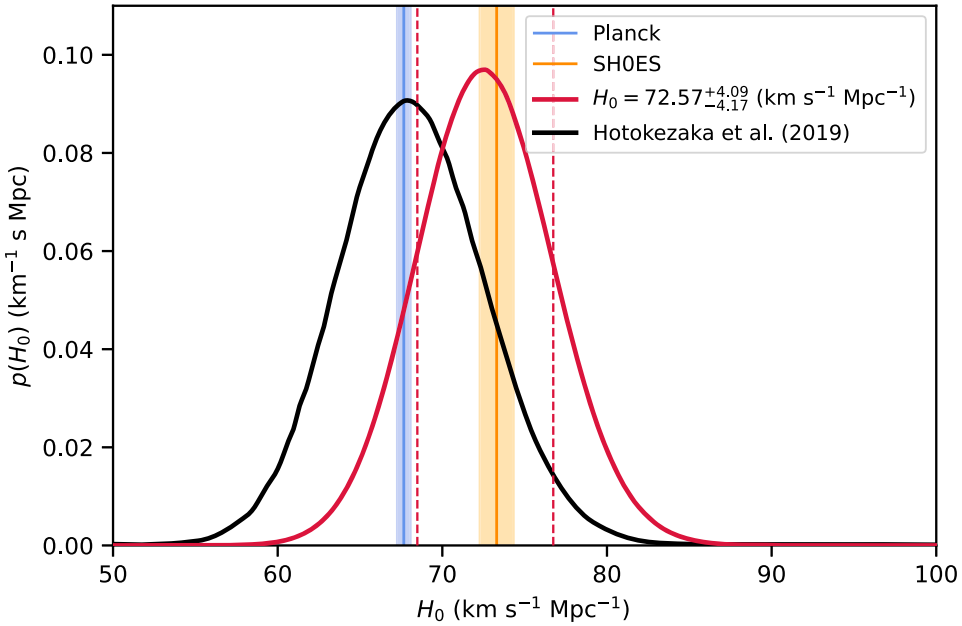

Figure 3. The Hubble constant inferred with the data of GW170817/GRB 170817A. The red solid line represents the H_0 estimated in `JetFit` model ($H_0 = 72.57^{+4.09}_{-4.17}$ km s^{-1} Mpc^{-1}) and the black solid line represents the result from Hotokezaka et al. (2019), while the blue and yellow regions represent the measurement results of Planck (67.66 ± 0.42 km s^{-1} Mpc^{-1}) and SHOES (73.30 ± 1.04 km s^{-1} Mpc^{-1}), respectively.

Hubble's Law. The bright BNS merger event GW170817 has been identified in NGC 4993, so the Hubble flow velocity can be measured. After fitting the multiwavelength light curves with the model developed by Wu & MacFadyen (2018), the viewing angle θ_v is constrained to $0.53^{+0.01}_{-0.01}$ rad ($\theta_v = 0.51^{+0.01}_{-0.02}$), which partially breaks the degeneracy between ι and d_L and improves the accuracy of d_L estimation in GW data analysis. Therefore, we finally obtain the estimation of the Hubble constant as $H_0 = 72.57^{+4.09}_{-4.17}$ km s^{-1} Mpc^{-1} ($H_0 = 71.80^{+4.15}_{-4.07}$ km s^{-1} Mpc^{-1}) from GW170817/GRB 170817, which is more consistent with the SHOES result rather than the CMB result. However, the uncertainty is still too large to confirm the Hubble tension. In our modeling, the possible kilonova afterglow component has been taken into account. In the `JetFit` model, the contribution of such a new component is not significant. In the `Afterglowpy` Gaussian structured jet model, the kilonova afterglow is more prominent and dominates the observed flux at $t \geqslant 700$ days. This distinction most likely arises from the different treatments on the sideways expansion. The `Afterglowpy` assumes the expansion spreads at sound speeds (Ryan et al. 2020), while the `JetFit` model has a slower speed based on relativistic hydrodynamical jet simulations. Therefore, in the `JetFit` scenario, the deceleration of the GRB ejecta will be less prominent than the case of `Afterglowpy` (Kumar & Granot 2003; van Eerten et al. 2012; Wu & MacFadyen 2018). Consequently, the GRB afterglow emission decline is shallower for `JetFit` and the contribution of the kilonova afterglow component is suppressed. Therefore, more data are needed to convincingly establish the presence of a kilonova afterglow.

With the improvement of multiband telescopes and the upgrade of GW interferometers, it is expected to detect more neutron star mergers with multimessengers. Chen et al. (2018) have predicted that the H_0 measurement will reach 2% precision within 5 yr based on the standard siren method. And the combination of the posterior distribution of H_0 estimation can reduce the error of H_0 to $\sigma_{H_0}/\sqrt{N}$ with N bright GW events, where σ_{H_0} is the typical width of the H_0 measurement. As shown in Saleem (2020) and Patricelli et al. (2022), the number of multimessenger detections of BNS mergers will be close to the single digits during O4/O5 because the large d_L restricts the detection of GW signal and the large θ_v restricts the GRB detection meanwhile. Since GW170817 is very close to us, its off-axis afterglow emission is still detectable in quite a few years. However, it is not the case for more distant events as expected. Fortunately, the afterglow emission would be much brighter for the on-axis events. More importantly, the jet opening angle, as well as its uncertainty, can be reliably estimated, with which both the d_L and H_0 can be well constrained (~3% accuracy) even with a single BNS merger (Wang et al. 2022). In view of the above facts, we conclude that more precise H_0 is expected with the GW standard sirens in the near future, and the Hubble tension will be credibly clarified.

We thank the anonymous referee for very helpful comments and suggestions. Y.-Y.W. thanks S.-J.G. for the help in improving the computational efficiency of the codes and for the valuable suggestions. This work was supported in part by NSFC under grants Nos. 11921003, 12225305, and 12233011. This research has made use of data and software obtained from the Gravitational Wave Open Science Center https://www.gw-openscience.org, a service of LIGO Laboratory, the LIGO Scientific Collaboration, and the Virgo Collaboration. LIGO is funded by the U.S. National Science Foundation. Virgo is funded by the French Centre National de Recherche Scientifique (CNRS), the Italian Istituto Nazionale della Fisica Nucleare (INFN), and the Dutch Nikhef, with contributions by Polish and Hungarian institutes.

Software: `Afterglowpy` (Ryan et al. 2020; https://pypi.org/project/afterglowpy/), `JetFit` (Wu & MacFadyen 2018, https://github.com/NYU-CAL/JetFit), `Bilby` Ashton et al. 2019; version 1.0.4; https://git.ligo.org/lscsoft/bilby/),

Pymultinest (Buchner 2016; version 2.11; https://pypi.org/project/pymultinest/), Dynesty (Speagle 2020; version 1.1; https://dynesty.readthedocs.io/en/latest/).

Appendix
The Posterior Distributions of the GRB and Kilonova Afterglow Parameters

Here, we present some posterior distributions of the GRB and kilonova afterglow parameters mentioned in Section 4. As an extra supplement for previous discussions, Figure 4 shows four scenarios, including the JetFit model without the constraint of the superluminal motion, the Gaussian structured jet model without the lateral spreading, the Gaussian structure jet model with fitting data during the first 200 days only, and the power-law structured jet. The first scenario yields a high $\ln Z$ (the same as the JetFit model with the constraint of the superluminal motion) but would predict an even higher H_0 because of the suggested $\theta_v \sim 0.6$ rad. The last three scenarios have significantly lower $\ln Z$ (represented in Figure 4) because of the poorer fits to the data. In Figure 5, we plot the posterior distributions of the parameters of kilonova afterglow modeling displayed in Figure 1. The spherical cocoon model, which describes the evolution of the kilonova afterglow approximately, specifies that the energy-velocity distribution follows a power-law distribution $E(u) = E_0(u/u_{\rm max})^{-k}$, where u is the dimensionless 4 velocity and within $(u_{\rm min}, u_{\rm max})$. In this framework, the shock driven by the kilonova blast wave is refreshed by the coasting of the slow material when it decelerates.

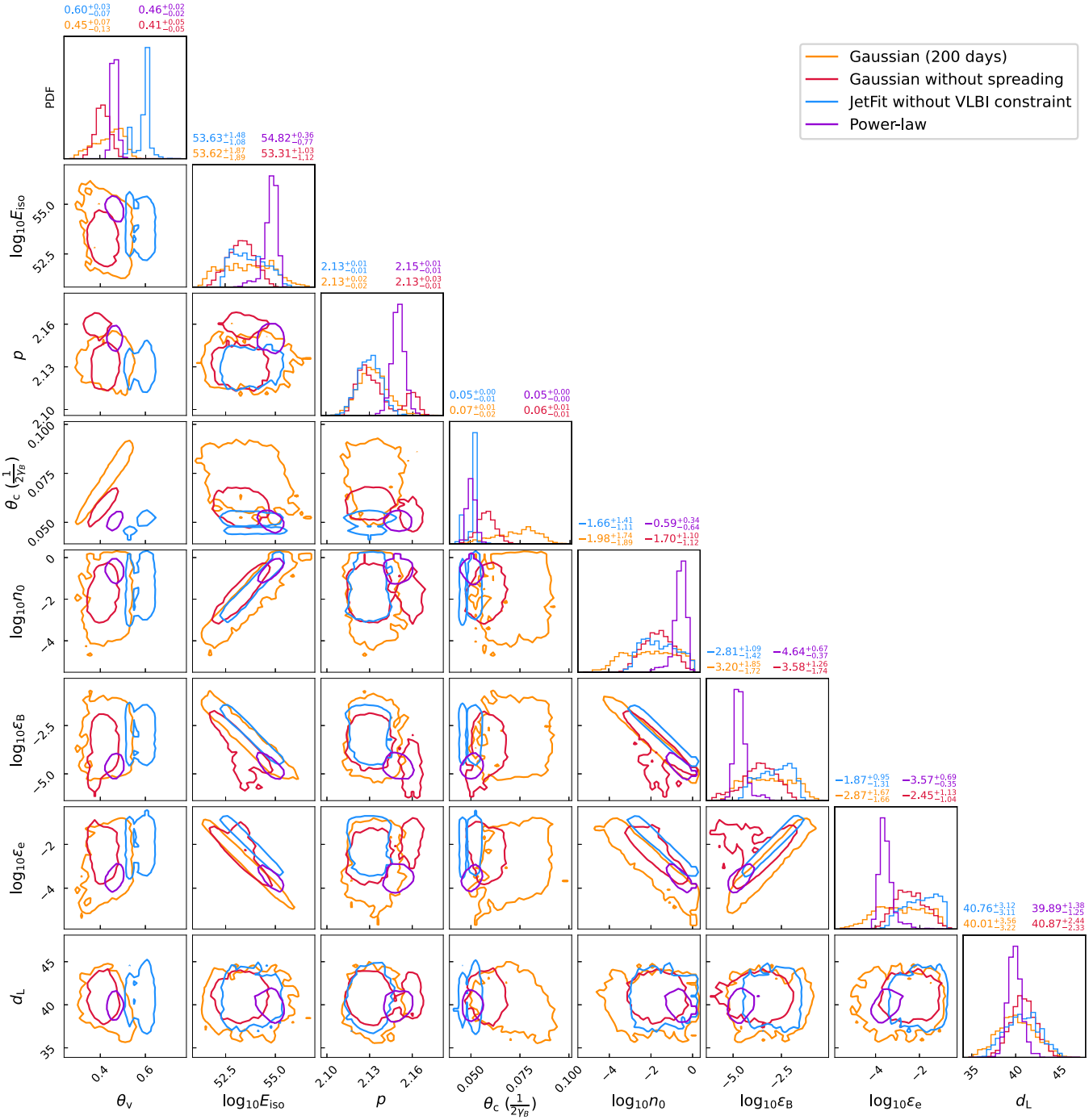

Figure 4. The posterior distributions of the parameters of four afterglow modeling. The `JetFit` model without the constraint of the superluminal motion ($\ln Z = 596$), the Gaussian model without lateral spreading ($\ln Z = 553$), and the power-law model ($\ln Z = 546$) are represented in blue, red, and purple, respectively. The Gaussian model just with the first 200 day observation data ($\ln Z = 301$) is also shown in orange for comparison. In these scenarios, the kilonova afterglow component has been taken into account. All of the ranges are at the 90% credible level.

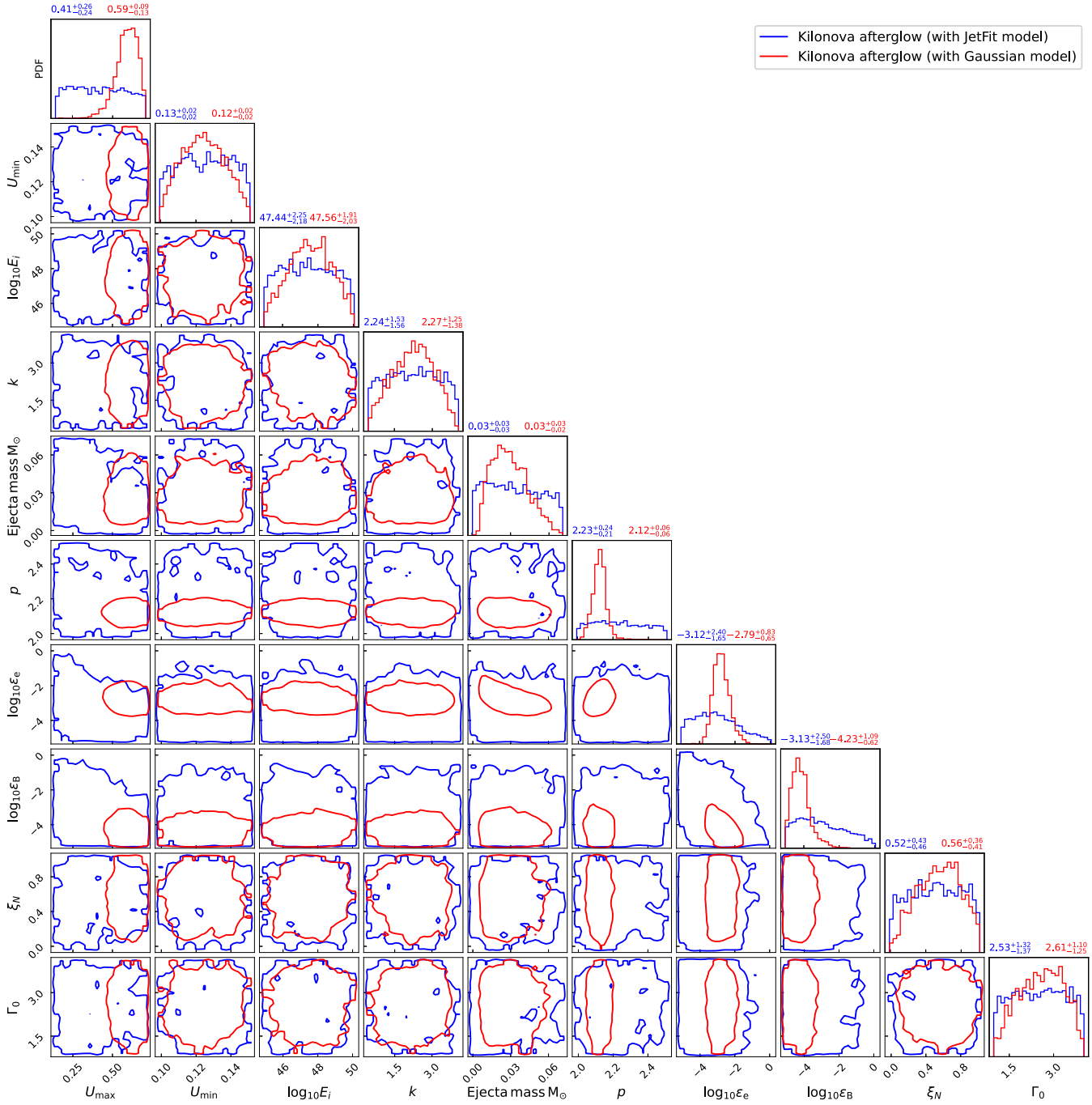

Figure 5. The posterior distributions of some parameters of kilonova afterglow modeling (see Figure 1 for the reproduced light curves). Note that the posterior distributions of the circumburst density n_0 and the luminosity distance $d_{\rm L}$ have already been presented in Figure 2. The ranges are at the 90% credible level.

ORCID iDs

Yi-Ying Wang https://orcid.org/0000-0003-1215-6443
Shao-Peng Tang https://orcid.org/0000-0001-9120-7733
Zhi-Ping Jin https://orcid.org/0000-0003-4977-9724
Yi-Zhong Fan https://orcid.org/0000-0002-8966-6911

References

Abbott, B. P., Abbott, R., Abbott, T. D., et al. 2017a, Natur, 551, 85
Abbott, B. P., Abbott, R., Abbott, T. D., et al. 2017b, ApJL, 848, L12
Abbott, B. P., Abbott, R., Abbott, T. D., et al. 2019, PhRvX, 9, 011001
Abbott, T. M. C., Abdalla, F. B., Annis, J., et al. 2018, MNRAS, 480, 3879
Alexander, K. D., Margutti, R., Blanchard, P. K., et al. 2018, ApJL, 863, L18
Ashton, G., Hubner, M., Lasky, P. D., et al. 2019, ApJS, 241, 27
Buchner, J. 2016, PyMultiNest: Python interface for MultiNest, Astrophysics Source Code Library, ascl:1606.005
Chen, H.-Y., Fishbach, M., & Holz, D. E. 2018, Natur, 562, 545
Dainotti, M. G., De Simone, B., Schiavone, T., et al. 2021, ApJ, 912, 150
Dainotti, M. G., De Simone, B., Schiavone, T., et al. 2022, Galax, 10, 24
D'Avanzo, P., Campana, S., Salafia, O. S., et al. 2018, A&A, 613, L1
Dietrich, T., Coughlin, M. W., Pang, P. T. H., et al. 2020, Sci, 370, 1450
Dietrich, T., Khan, S., Dudi, R., et al. 2019, PhRv, 99, 024029
Dobie, D., Kaplan, D. L., Murphy, T., et al. 2018, ApJL, 858, L15
Duan, K.-K., Jin, Z.-P., Zhang, F.-W., et al. 2019, ApJL, 876, L28
Fong, W., Blanchard, P. K., Alexander, K. D., et al. 2019, ApJL, 883, L1
Ghirlanda, G., Salafia, O. S., Paragi, Z., et al. 2019, Sci, 363, 968
Hajela, A., Margutti, R., Alexander, K. D., et al. 2019, ApJL, 886, L17
Hajela, A., Margutti, R., Bright, J. S., et al. 2022, ApJL, 927, L17

Hallinan, G., Corsi, A., Mooley, K. P., et al. 2017, Sci, 358, 1579
Han, M.-Z., Huang, Y.-J., Tang, S.-P., & Fan, Y.-Z. 2022, arXiv:2207.13613
Hotokezaka, K., Nakar, E., Gottlieb, O., et al. 2019, NatAs, 3, 940
Howlett, C., & Davis, T. M. 2020, MNRAS, 492, 3803
Huang, Y., Chen, H.-Y., Haster, C.-J., et al. 2022, arXiv:2204.03614
Jin, Z.-P., Li, X., Wang, H., et al. 2018, ApJ, 857, 128
Kathirgamaraju, A., Giannios, D., & Beniamini, P. 2019, MNRAS, 487, 3914
Kumar, P., & Granot, J. 2003, ApJ, 591, 1075
Lamb, G. P., Lyman, J. D., Levan, A. J., et al. 2019, ApJL, 870, L15
Lange, J., O'Shaughnessy, R., & Rizzo, M. 2018, arXiv:1805.10457
Lin, H., Totani, T., & Kiuchi, K. 2019, MNRAS, 485, 2155
Lyman, J. D., Lamb, G. P., Levan, A. J., et al. 2018, NatAs, 2, 751
Makhathini, S., Mooley, K. P., Brightman, M., et al. 2021, ApJ, 922, 154
Margutti, R., Alexander, K. D., Xie, X., et al. 2018, ApJL, 856, L18
Mooley, K. P., Deller, A. T., Gottlieb, O., et al. 2018a, Natur, 561, 355
Mooley, K. P., Frail, D. A., Dobie, D., et al. 2018b, ApJL, 868, L11
Mooley, K. P., Nakar, E., Hotokezaka, K., et al. 2018c, Natur, 554, 207
Mukherjee, S., Lavaux, G., Bouchet, F. R., et al. 2021, A&A, 646, A65
Nathanail, A., Gill, R., Porth, O., Fromm, C. M., & Rezzolla, L. 2021, MNRAS, 502, 1843
Nedora, V., Radice, D., Bernuzzi, S., et al. 2021, MNRAS, 506, 5908
O'Connor, B., & Troja, E. 2022, GCN, 32065, 1
Patricelli, B., Bernardini, M. G., Mapelli, M., et al. 2022, MNRAS, 513, 4159
Piro, L., Troja, E., Zhang, B., et al. 2019, MNRAS, 483, 1912
Planck Collaboration, Aghanim, N., Akrami, Y., et al. 2020, A&A, 641, A6
Resmi, L., Schulze, S., Ishwara-Chandra, C. H., et al. 2018, ApJ, 867, 57
Riess, A. G., Yuan, W., Macri, L. M., et al. 2022, ApJL, 934, L7
Ryan, G., Eerten, H. v., Piro, L., & Troja, E. 2020, ApJ, 896, 166
Saleem, M. 2020, MNRAS, 493, 1633
Sarin, N., Omand, C. M. B., Margalit, B., & Jones, D. I. 2022, MNRAS, 516, 4949
Schutz, B. F. 1986, Natur, 323, 310
Speagle, J. S. 2020, MNRAS, 493, 3132
Troja, E., Piro, L., van Eerten, H., et al. 2017, Natur, 551, 71
Troja, E., Piro, L., Ryan, G., et al. 2018, MNRAS, 478, L18
Troja, E., van Eerten, H., Ryan, G., et al. 2019, MNRAS, 489, 1919
Troja, E., van Eerten, H., Zhang, B., et al. 2020, MNRAS, 498, 5643
Troja, E., O'Connor, B., Ryan, G., et al. 2022, MNRAS, 510, 1902
van Eerten, H., van der Horst, A., & MacFadyen, A. 2012, ApJ, 749, 44
Verde, L., Treu, T., & Riess, A. G. 2019, NatAs, 3, 891
Wang, H., & Giannios, D. 2021, ApJ, 908, 200
Wang, Y.-Y., Tang, S.-P., Li, X.-Y., Jin, Z.-P., & Fan, Y.-Z. 2022, PhRvD, 106, 023011
Wu, Y., & MacFadyen, A. 2018, ApJ, 869, 55